3D printed nanofiltration composite membranes with reduced concentration polarization

Saeed Mazinani, Abouther Al-Shimmery, Y.M. John Chew, Davide Mattia
Department of Chemical Engineering, Centre for Advanced Separations Engineering, University of Bath, Claverton Down, Bath BA2 7AY, UK

Abstract

3D printed nanofiltration (NF) composite membranes with surface patterns minimising the impact of concentration polarisation (CP) are presented here for the first time. The membranes consist of a NF polydopamine-coated polyvinylidene fluoride (PVDF/PDA) selective layer on a 3D printed asymmetric wavy (patterned) support. The result is a wavy composite membrane with pure water permeance of 14 ± 2 LMH bar^{-1} and molecular weight cut-off of ~550 Da, measured using a crossflow NF setup at a transmembrane pressure of 2 bar for Reynold number (*Re*) of 700, using a range of dyes (mass balance > 97% for all tests). The CP behaviour of the composite membranes was assessed by filtration of Congo red (CR) dye solution (0.01 g L^{-1}), showing that the wavy pattern significantly reduced the impact of CP compared to the flat membranes, with a nearly tripling of the mass transfer coefficient and a 57% decline of the CP factor. Computational fluid dynamics showed that these significant performance improvements were due to improved hydrodynamics, with the maximum surface shear stress induced by the wavy structure (1.35 Pa) an order of magnitude higher than that of the flat membranes (0.18 Pa) at *Re* = 700. These results demonstrate that 3D printing is a viable technology route to reducing concentration polarisation in membrane nanofiltration applications.

Keywords: 3D printing, CFD simulation, Wavy composite membrane, 3D asymmetric support, Concentration polarization.

1. Introduction

Concentration polarization (CP) occurs when non-interacting solutes build up near the membrane-feed interface, resulting in a higher solute concertation than that in the bulk solution [1]. This build up can induce water flux decline, reduce quality of produced water, increase power consumption and operating costs in membrane-based water treatment [2, 3], including reverse osmosis (RO) and nanofiltration (NF) processes [4, 5]. Numerous attempts have been made to reduce the impact of CP through modification of the membranes, e.g. surface coating [6], grafting [7] and interfacial polymerization [8]. However, these measures have shown limited success since they also negatively impact membrane flux and, moreover, the uncertainty around their long-term stability and scalability has resulted in their low uptake [9]. Therefore, there is intense interest in methods that would effectively reduce CP without negatively affecting permeance and ensuring stable performance over time.

The patterning of membranes' surfaces has been extensively explored as a potential route to minimise CP and fouling by altering the membrane's surface topography [10, 11]. Micrometre-scale surface patterns can effectively reduce the build-up of CP layer by promoting fluid shear stress on the membrane surface, while at the same time enhance permeance by increasing the effective filtration area [12, 13]. It was demonstrated that a patterned membrane can lead to a reduction in energy consumption of up to 88% compared to a flat one with the same rejection [14]. However, the actual use of patterned membranes has been limited due to insufficient fidelity and flexibility of current patterning methods, e.g. stamping, moulding or nanoimprinting, as they negatively affect permeance and durability of the membranes [15].

Additive manufacturing, known as three-dimensional (3D) printing can produce well-defined patterned membranes with more complex patterns in a single process that are impossible to manufacture otherwise [16]. One of the most versatile 3D printing technique that is used in membrane fabrication for liquid-based filtration is multi-jet printing (MJP). MJP offers a high resolution, in the order of few micrometres, and is able to create complex parts via the controlled deposition of light-curable resins [17]. During the fabrication process using this technique, the 3D printer utilizes two polymeric materials, one to build the structure and the other as support, which is subsequently removed. Although there are many research studies on the advancement of 3D printers, only few of them have used 3D printing to fabricate patterned membranes, and all of which employed symmetric substrates [18].

Poly(vinylidene fluoride) (PVDF) membranes are widely used in water and wastewater treatment applications due to their high mechanical and chemical stability along with good

processability [19]. Commercially available in microfiltration (MF) and ultrafiltration (UF) ranges, PVDF membranes, due to their hydrophobicity, are generally hydrophilized for better performance [20]. PVDF UF composite membranes have been prepared via coating of hydrophilic polydopamine (PDA) over MF and loose UF PVDF membranes as support [21-23]. There is, however, no study on preparation of PVDF NF composite membranes in the literature.

This work demonstrates the fabrication via 3D printing of NF composite membranes with a wavy pattern, resulting in reduced CP build-up. The asymmetric wavy supports were first carefully designed to enable the fabrication of thin supports with higher intrinsic permeability, and better mechanical stability compared to symmetric supports [18]. The structural design parameters of the wavy supports were optimised integrating computational fluid dynamics (CFD) simulations with material characterization. A multi-jet 3D printer was then used to print asymmetric supports. NF selective layers were prepared by coating a polydopamine (PDA) layer over as-prepared UF PVDF membranes. The NF PVDF/PDA selective layers were then applied onto the asymmetric supports via vacuum filtration to fabricate 3D printed NF composite membranes. The MWCO of the composite membranes was determined via dye rejection tests using a cross-flow NF setup at 2 bar. The dye CP behaviour of the composite membranes was assessed by filtration of Congo red dye solution through determination of time-dependent maximum solute concentration, and calculation of mass transfer coefficient and CP factor. The results were compared with a 3D NF flat composite membrane as a reference.

2. Materials and methods

2.1. Materials

A commercial 3D printer (ProJet 3500 HD Max printer, *3D Systems*, USA) was used to fabricate the asymmetric membrane supports, using proprietary urethane acrylate (VisiJet® M3-X, *3D Systems*, USA) and a support wax (VisiJet® S300, *3D Systems*, USA). PVDF (Kynar 761, Mw = 634,000 g mol^{-1}, *Arkema*), N-Methyl-2-pyrrolidone (NMP, purity > 99%, *Acros*), dopamine hydrochloride (DPA, purity > 98%, *Sigma-Aldrich*) and Trizma hydrochloride (TRIS HCl, purity > 99%, *Sigma-Aldrich*) were used to prepare selective layer. Reactive black 5 (RB5, MW = 991 g mol^{-1}, *Sigma-Aldrich*), Congo red (CR, MW = 697 g mol^{-1}, *Sigma-Aldrich*), acid red 1 (AR1, MW = 509 g mol^{-1}, *Sigma-Aldrich*) and methyl orange (MO, MW = 327 g mol^{-1}, *Sigma-Aldrich*) were used as model dyes in the cross-flow nanofiltration experiments. Sodium sulphate (Na_2SO_4, purity > 99%, *Sigma-Aldrich*) was used to prepare the

salt solution for the concentration polarisation studies. All the solutions used in this work were prepared using deionized water (DI, Purelab®, Elga*Veolia*).

2.2. Preparation of the 3D printed nanofiltration composite membranes

The fabrication procedure for the 3D printed nanofiltration (NF) composite membranes comprises three main steps: (i) Fabrication of the asymmetric supports using 3D printing; (ii) preparation of the NF selective layer; and (iii) application of the NF selective layer onto the 3D printed supports.

2.2.1. Fabrication of the asymmetric supports using 3D printing

The asymmetric support consists of a single 3D printed object, comprising two sections, a top dense layer (50 µm thickness) and a bottom one (200 µm thickness) with straight-through cylindrical pores (**Figure 1**). The asymmetric design actually improves the mechanical stability of the support and enables the fabrication of the supports with lower overall thickness and larger pore diameter in the bottom layer compared to the symmetric case [18]. This led to an increase in the support's intrinsic permeability and eased removal of the wax support material [24]. The asymmetric support was designed using OpenSCAD, using a procedure reported previously [18].

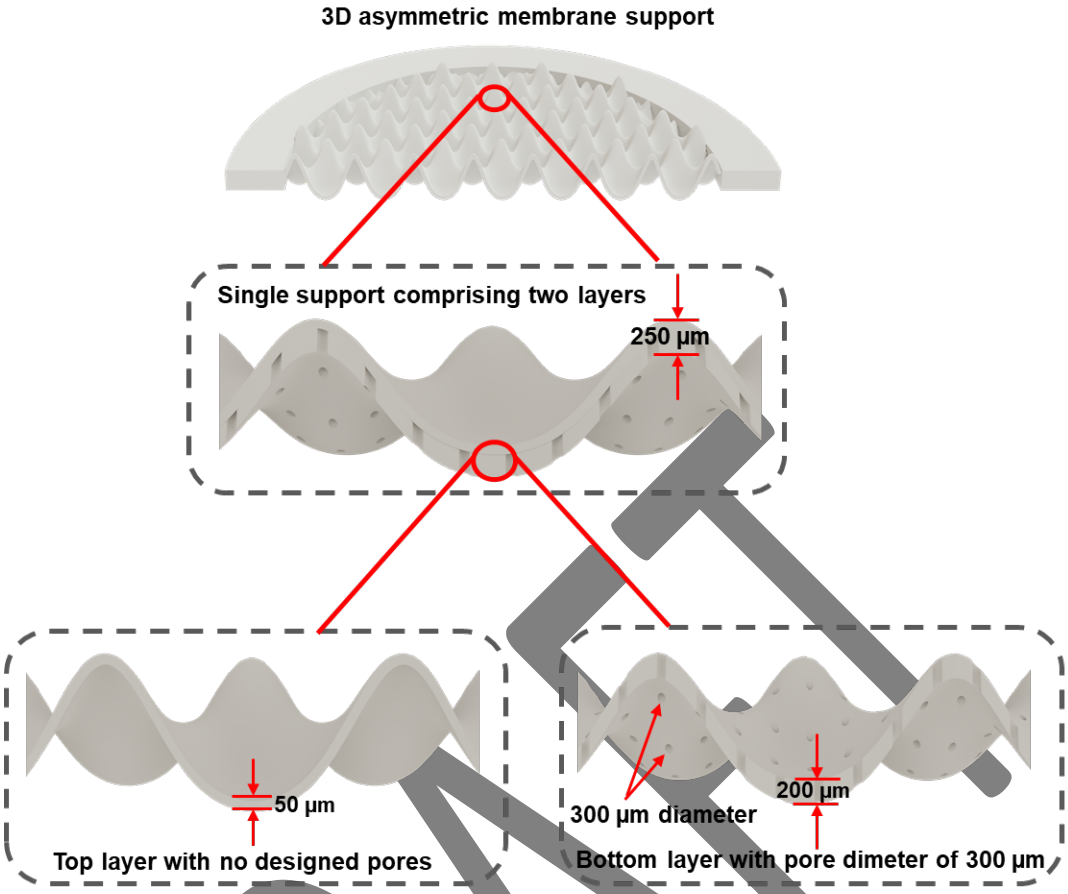

Figure 1. The 3D asymmetric support consists of a single 3D printed object, comprising two sections, a top dense one (50 µm thickness) and a bottom one (200 µm thickness) with straight-through cylindrical pores of 300 µm.

The pores were designed with 300 µm diameter and 200 µm interpore distance using Autodesk Inventor Professional 2016 and superimposed on the wavy surface (37 mm diameter) of the bottom section. Thereafter, the two sections were merged into a single digital object and a rim (6.5 mm wide) was added around the circular wavy area to generate an asymmetric support with 50 mm overall diameter. The final computer-aided design (CAD) file was subsequently converted into the stereolithography (STL) format using OpenSCAD and transferred to the 3D printer using 3D Sprint software (2.0, *3D systems*, USA). The flat supports were designed using the same procedure. The final post-treatment step was to remove the wax from inside the pores of the subsection using EZ Rinse-C oil [18].

2.2.2. Preparation of NF selective layer

The NF selective layer was obtained by coating PDA over an UF PVDF membrane. To prepare a dope solution, PVDF (17.5 wt%) was first dissolved in NMP and then stirred using a roller

mixer (120 VAC, *Cole-Parmar*) for two days. The dope solution was then left overnight to degas. The bubble-free solution was cast on top of a clean glass plate at room temperature using a casting knife with 50 μm gap height under ~35% relative humidity (**Figure 2(a)**). After 15 s of exposure to air, the glass plate was immersed in a DI water bath at room temperature to complete the phase inversion process. The DPA solution (2 g L^{-1}, pH~8, 300 ml) preparation involved first dissolution in DPA in TRIS HCl solution (pH = 8.5, 10 mM, 200 ml), followed by pH adjustment to 8.5 by addition of sodium hydroxide solution (NaOH, 10 mM, 100 ml). The as-prepared PVDF membrane was cut 6 cm diameter discs and placed into a customised membrane holder so that only its front side was exposed to the coating solution. Subsequently, the fresh DPA was poured into the membrane holder and continuously stirred using an overhead stirrer for 24 h at room temperature. The DPA solution was then replaced with fresh solution and the membrane was exposed to the fresh solution for another 24 h. The interaction between PVDF and DPA forms a thin PDA layer on the PVDF surface through oxidant self-polymerization [25, 26], resulting in a NF selective layer (**Figure 2(a)**). Thereafter, the NF selective layer was removed from the membrane holder and rinsed with water for 30 mins to remove unreacted PDA particles. The resultant membrane was stored in DI water before further use.

2.2.3. Preparation of 3D printed NF composite membranes

The NF PVDF/PDA selective layer was first applied onto the 3D support, followed by vacuum filtration with DI water for at least 3 h to ensure adhesion of the selective layer on the 3D printed support, resulting in the formation of wavy or flat 3D composite membranes (**Figure 2(b)**).

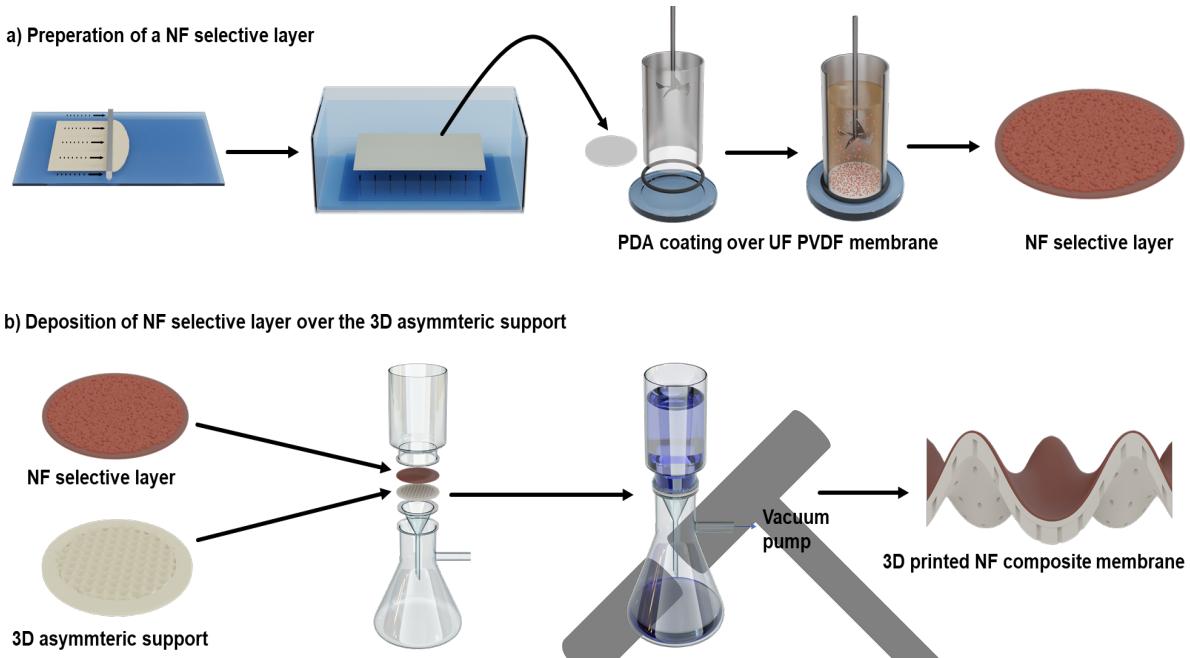

Figure 2. Schematic of the preparation of wavy 3D composite membranes: (a) preparation of NF selective layer by coating a PDA layer over a UF PVDF membrane, (b) NF selective layer deposition over the 3D support via vacuum filtration.

2.3. Characterisation of 3D composite membrane

A scanning electron microscope (SEM, JEOL SEM6480LV, Japan) along with a digital microscope (VHX-6000, *Keyence*, Japan) were used to investigate the morphology of the 3D support, selective layer, and 3D composite membrane. Membrane samples were first dried under vacuum (~40 ºC) overnight and then sputter-coated with 10 nm of chromium (Edwards Sputter Coater S150B, *Mechatech Systems*, UK) for SEM imaging.

To characterise chemical bonds on the surface of the selective layer, an ATR-FTIR spectrometer (Frontier, *PerkinElmer*, Germany) was used. The spectra were collected as a result of 16 running scans at a resolution of 4 cm^{-1} within the 600 cm^{-1} to 4000 cm^{-1} wavelength range.

The surface chemical composition of the selective layer was analysed by X-ray photoelectron spectroscopy (XPS, K-alpha, *Thermo Fisher Scientific*) using Al Kα as the radiation source over an area of around 400 µm. Data was collected at pass energies of 150 eV and 40 eV for survey (1 eV step size) and high (0.1 eV step size) resolution scans, respectively.

The water contact angle of the support, selective layer, and composite membrane was determined using a contact angle goniometer (OCA20, *DataPhysics Instruments*, Germany) in sessile mode at room temperature, using 5 µl droplets. The reported values are the average of at least 10 measurements.

The surface roughness of the 3D supports was assessed using a digital microscope (VHX-6000, *Keyence*, Japan) over scan areas of 100 × 100 µm. The surface roughness of the selective layer was analysed using atomic force microscopy (AFM, *Bruker Multimode IIIA*, USA) over scan areas of 5 × 5 µm in the tapping mode (time/line = 1 s, samples/line = 256).

A Zetasizer Nano (ZS, Malvern Instruments Ltd.) was used to measure the surface zeta potential of membrane samples at neutral pH = 7.0. The reported values are the average of at least three measurements.

2.4. Filtration performance and CP characterisation

The filtration performance and CP behaviour of the composite membranes was evaluated using a cross-flow NF setup (**Figure S2**) described previously [18]. All experiments were carried out at crossflow velocity of 0.1 ms^{-1} (corresponding to Re = 700) at TMP of 2 bar for 30 minutes, following a pre-compaction step at 3 bar for 24 h using pure water. The permeance (K, LMH bar^{-1}) of the membranes was calculated via the following:

$$K = \frac{V}{\Delta t \cdot A \cdot \Delta p} \quad (1)$$

where V is the permeate volume (m^3), Δt is time (hr), A is the effective membrane area (m^2), and Δp is the transmembrane pressure (bar). The effective filtration areas for the flat and wavy asymmetric supports are 1074 and 1288 mm^2, respectively, calculated using 3D Sprint (*3D Systems*, USA) software [24].

The dye rejection of the membranes was calculated using equation (2):

$$R\ (\%) = \frac{C_F - C_P}{C_F} \quad (2)$$

where C_F and C_P represent the solute concentration in the feed and permeate, respectively.

Dye concentration was measured using a UV-Vis spectrophotometer (Cary, *Agilent*, USA). The mass balance in dye rejection tests was calculated using equation (3):

$$mass\ balance\ (\%) = \frac{C_p V_p + C_r V_r}{C_F V_F} \times 100 \quad (3)$$

where C_r is the retentate concentration (g L^{-1}), V_P, V_r, V_F represent the permeate, retentate and feed solutions volumes (L), respectively.

To assess the CP behaviour of the membranes, Congo red dye solution (0.01 g L^{-1}) was circulated through the setup and the membrane flux J_v (LMH) was measured. The mass transfer coefficient k (m s^{-1}) was calculated from equation (4) using the stagnant film model [27]:

$$k = \frac{J_v}{\ln\left(\frac{C_m - C_p}{C_F - C_p}\right)} \quad (4)$$

where J_v is the permeation flux (LMH), C_m is the maximum solute concentration at the membrane surface (g L^{-1}), C_p is the permeate concentration (g L^{-1}) and C_F is the feed concentration (g L^{-1}). C_F and C_p were calculated from experimental measurements while the concentration of dye at the membrane surface, C_m, was estimated using computational fluid dynamics (next section).

The CP factor, Γ, was determined using equation (5) [10]:

$$\Gamma = \frac{C_m - C_F}{C_F} \quad (5)$$

2.5. CFD simulations

To study flow and concentration fields over the surface of flat and wavy composite membranes, the conservation of mass and momentum equations along with mass transport equations for steady-state flow in the laminar flow regime, were numerically solved using Laminar Flow and Transport of Diluted Species interfaces of COMSOL Multiphysics (COMSOL 5.6, *Comsol Inc.*, USA) software. Two-dimensional (2D) simulation domains (**Figure S1**) were created to reproduce the cross section of the filtration cell with overall size of 4 mm × 50 mm (height × length) [18]. The wavy structure was set at amplitude α = 0.70 mm, and wavelength λ = 3 mm following optimisation. Further details of the simulation are reported in the **Supporting Information**.

CFD modelling was also used to simulate the permeance decline as a function of time for the dye solution. This was then used to determine the local concentration of the dye at the membrane surface, C_m, which, in turn, allowed calculating the mass transfer coefficient in

equation (4). The simulated flux decline was compared to experimental profiles, with an excellent match, discussed below. The CFD model has been previously validated using BSA by the authors [18] and independently [28].

3. Results and discussion

3.1. Design and optimisation of 3D printed composite membranes

The optimisation process of the 3D printed wavy composite membranes has been described previously [18]. A combination of CFD simulations along with material characterisation was employed to optimise the wavy structure parameters including amplitude (α), and wavelength (λ). Several wavy supports with certain amplitude and wavelength were first fabricated using the 3D printer and their morphology was then characterised using SEM and digital microscope to identify a range for amplitude (α, 0-1.50 mm) and wavelength (λ, 0-12 mm) compatible with the printing process. The minimum thickness of the wavy support is dictated by its mechanical properties where below a certain thickness the support can no longer withstand any significant pressure. For symmetric supports the minimum thickness was found to be 500 µm whereas asymmetric design allowed reducing the minimum thickness to 250 µm, thereby reducing support resistance and material consumption. Moreover, the asymmetric support having no pores in the top prevents the selective layer from breaking during vacuum filtration which as observed for symmetric wavy supports.

The fluid flow around the wavy surface in terms of surface shear stress and vortex pattern was analysed using CFD simulations. **Figure 3** shows a contour plot with different shear stress regions caused by the wavy structure based on printable values of amplitude and wavelength at Re = 700.

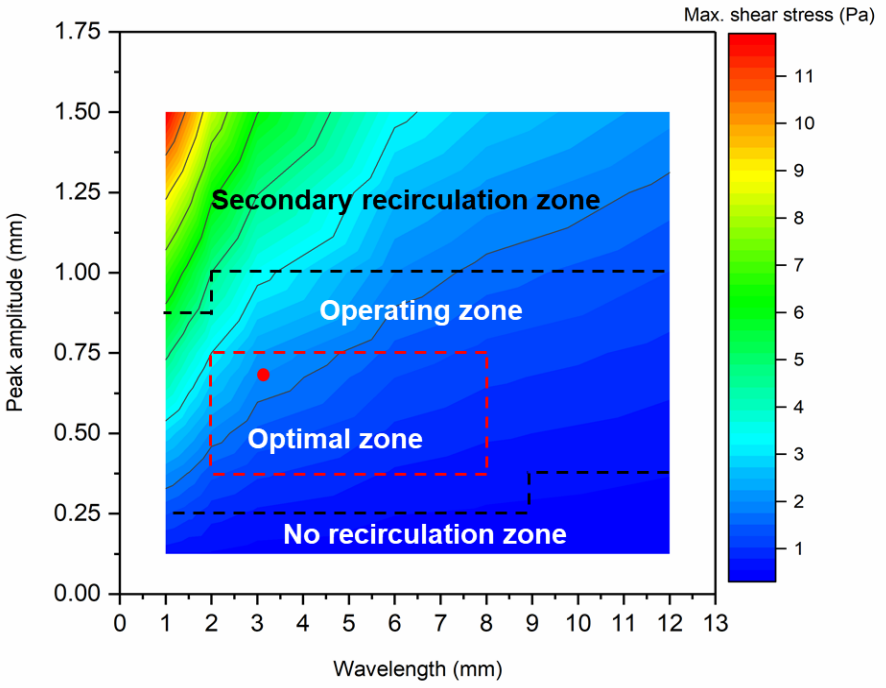

Figure 3. Contour plot with different shear stress regions caused by the wavy structure based on printable values of α and λ at *Re* = 700 using a 3D printed asymmetric support. The red dot represents the optimal fabrication parameters used in this work.

Wavy structures with large amplitudes and short wavelengths induce the highest fluid shear stress while small amplitudes and long wavelengths cause lowest shear stress. High shear stress and vortex formation at the membrane's surface enhance mass transfer coefficient and therefore reduce concentration polarisation [29]. Within the operating zone, materials considerations further limited the printable range for amplitude and wavelength: For $\alpha > 0.5$ mm, the selective layer prepared from polyethersulfone (PES) would be pierced-through during the vacuum-driven adhesion step. To improve the selective layer's conformability for larger α values, PVDF was selected to use as the main polymer for preparation of the selective layer due to its outstanding mechanical properties [30]. This systematic optimisation expanded the 'optimal zone', by raising the upper limit for α from 0.63 mm to 0.75 mm. In turn, higher α values result in higher shear stress, further reducing fouling. This optimisation process let to the selection of $\alpha = 0.70$ mm and $\lambda = 3$ mm to induce maximum shear stress (represented by the red dot in **Figure 3**) over the membrane surface. By using PVDF as the selective layer, it was possible to increase the amplitude α by 40% from 0.5 mm to 0.7 mm, resulting in approximately doubling the shear stress from 0.7 Pa to 1.35 Pa, compared to 0.18 Pa for the flat 3D printed membrane ($\alpha = \lambda = 0$). An extensive discussion of the interplay between the

different parameters of the 3D printer, the selective layer and the hydrodynamic landscape has been reported elsewhere [18].

3.2. Characterization of the 3D printed support, selective layer, and 3D composite membrane

SEM micrographs of the 3D printed top dense section (**Figure 4a**) and bottom section with cylindrical pores with diameter of 300 µm (**Figure 4b**) show a highly regular structure with no defects and following the wavy structure design (cfr. **Figure 1**). Although the top layer is dense, i.e. there were no pores designed into this, there is nonetheless some porosity due to the resolution of the 3D printer itself, as previously observed for polysulfone membranes [31].

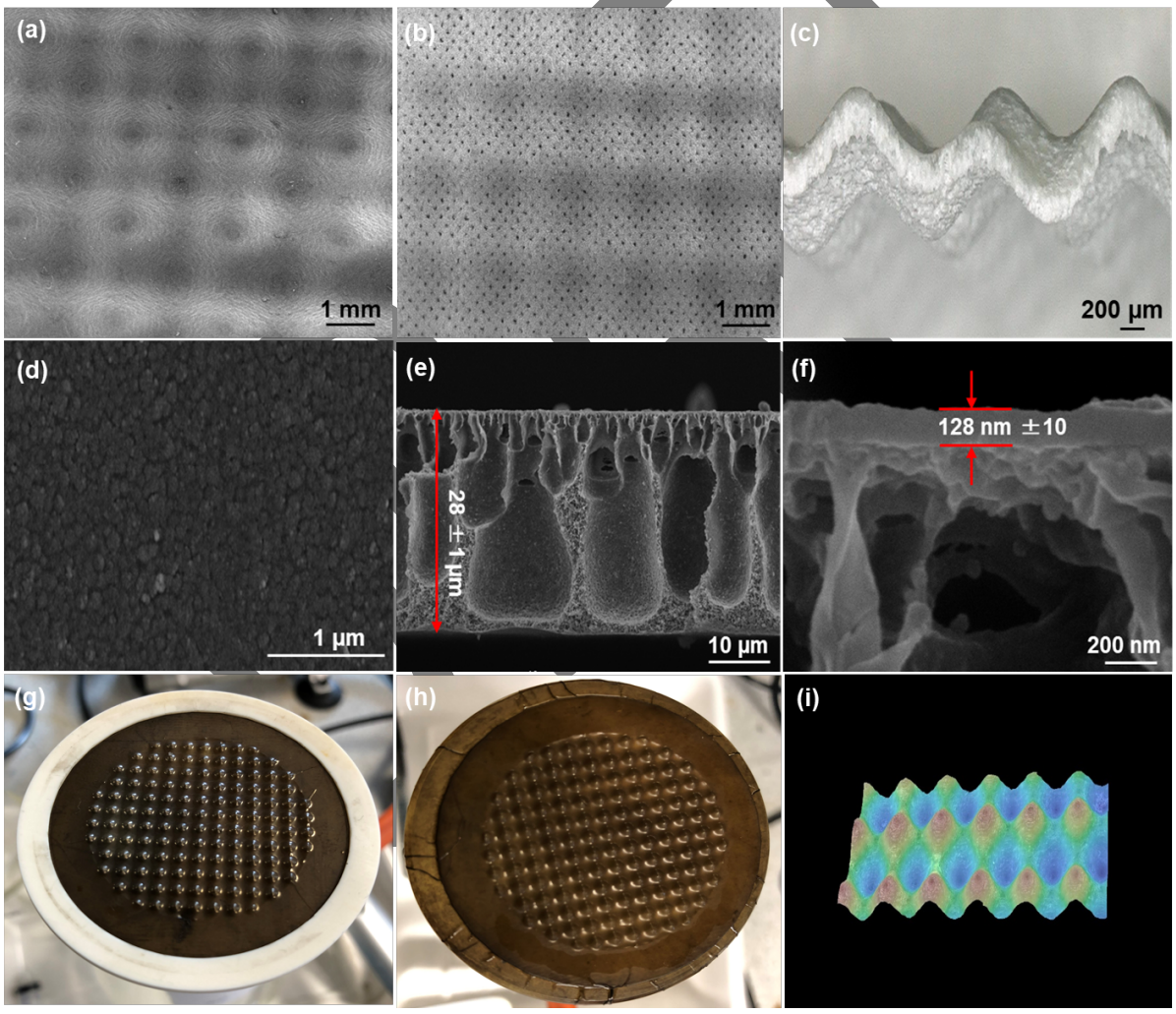

Figure 4. SEM micrographs of (a) top dense section, (b) bottom section (with pore diameter of 300 µm) of the asymmetric 3D printed wavy support; (c) digital micrograph of the cross-section of 3D printed wavy support; SEM micrographs of (d) surface, and cross section of the PVDF/PDA selective layer at (e) ×55K and (f) ×75K magnification; optical micrographs of 3D

wavy composite membrane from (g) top and (h) side, showing a conformal layer of the PVDF/PDA onto the wavy support; (i) digital micrograph of 3D wavy composite membrane.

Figure 4 (c) shows the cross section of the wavy support with no gaps between the two layers confirming the asymmetric support was successfully printed as a single continuous object with lower total thickness (~250 μm) and higher intrinsic permeability ($9 \pm 1 \times 10^{-12}$ m^2) compared to the symmetric supports [18]. The SEM micrographs of the surface and cross section of the PVDF/PDA selective layer are shown in **Figure 4 (d-f)**. The densely packed PDA particles can be clearly observed on the surface of the selective layer (**Figure 4(d)**). The deposition of PDA can lead to the formation of numerous nanostructured PDA aggregates formed from the non-covalent interactions between PDA oligomers [32]. The cross-section of the selective layer (**Figure 4e**) presents a typical asymmetric structure (overall thickness of 28 ± 1 μm) with a micro-void porous sublayer and a thin dense skin layer (average thickness of 128 ± 10 nm) formed from PDA (**Figure 4f**). A conformal adhesion between the PVDF/PDA selective layer and membrane support was confirmed using the optical micrographs and topographical image of the wavy 3D composite membrane (**Figure 4 (g-i)**).

The FTIR spectra of the (a) pristine PVDF (b) PVDF/PDA selective layer and (c) pristine PDA are reported in **Figure 5**. In the PVDF spectra, the characteristic peaks at 1403 cm^{-1} and 1181 cm^{-1} are attributed to CH_2 wagging vibration and C–C band, respectively, while the sharp peak at 873 cm^{-1} is assigned to C–C–C asymmetrical stretching vibration [33]. In the PVDF spectra, the characteristic peaks at 1403 cm^{-1} and 1181 cm^{-1} are attributed to CH_2 wagging vibration and C–C band, respectively, while the sharp peak at 873 cm^{-1} is assigned to C–C–C asymmetrical stretching vibration [33]. In the spectra of the coated PVDF membrane with PDA, three new peaks can be observed: A broad peak between 3100 cm^{-1} and 3600 cm^{-1} corresponds to N–H/O–H stretching vibrations of PDA, while the two small peaks at 1603 cm^{-1} and 1507 cm^{-1} are attributed to C=O and C=C/C=N bands, respectively, confirming a strong bond between PVDF and PDA [30].

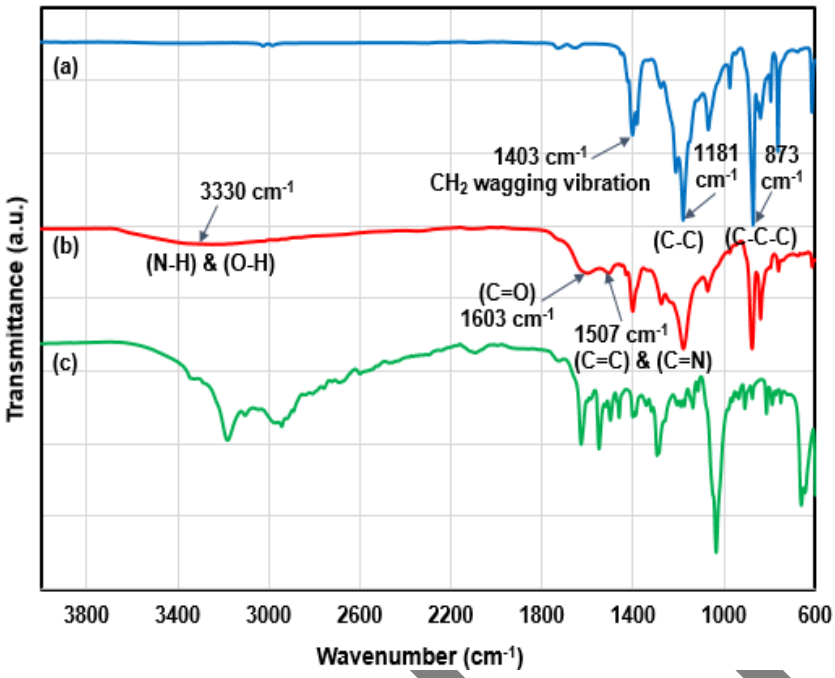

Figure 5. ATR-IR spectra of (a) pristine PVDF, (b) PVDF/PDA selective layer, and (c) pristine PDA.

The C1s XPS spectra along with surface atomic composition of pristine PVDF and PVDF/PDA membranes are shown in **Figure 6 (a)** and **(b)**, respectively. For the former, only C and F elements are present on the surface of pristine PVDF membrane, as expected. After coating with PDA, the atomic composition of C significantly increased, with signals appears for N and O elements appeared, and no detection of F, confirming the formation of a uniform coating. This data agrees well with the literature [30]. This was further confirmed looking at the C1s XPS spectra of pristine PVDF and PVDF/PDA membrane. For the pristine PVDF, only two peaks at binding energies of 284.6 eV (C-C) and 289.1 eV (C-F) are observed [34].

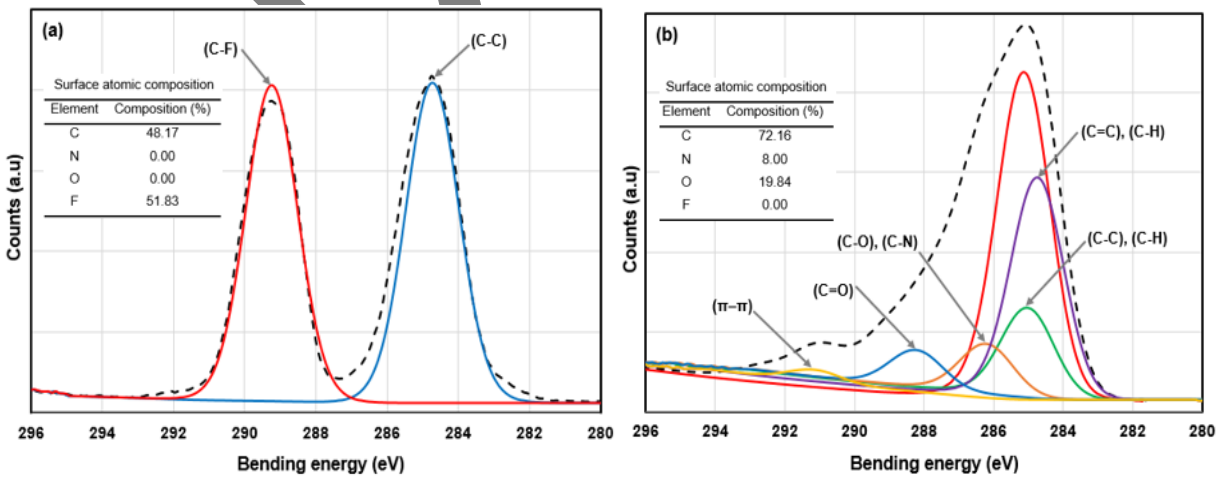

Figure 6. C1s X-ray photoelectron spectra of (a) pristine PVDF membrane and (b) PVDF/PDA membrane; the inset tables summarise the surface atomic composition.

In the C1s XPS spectra of the PVDF/PDA membrane, the C-F band has disappeared and new peaks appeared at binding energies of 284.6 eV (C=C/C-H), 285 eV (C-C/C-H), 286.3 eV (C-C/C-O), 288.1 eV (C=O), and 291.2 eV (π-π stacking) [30]. These new bands confirm the presence of PDA on the PVDF surface as PDA can adhere to polymeric surface through amino, imino, hydroxyl and catechol functional groups [35]. The O1s spectra of PVDF/PDA membrane can be found in **Figure S3**.

The properties of the 3D printed support, pristine PVDF, PVDF/PDA selective layer and 3D wavy composite membrane are reported in **Table 1**. The water contact angle of the pristine PVDF dropped from 93º to 51º after coating with PDA. This is attributed to the hydrophilic amine and catechol groups of PDA [23], further confirming the successful coating of PDA onto the PVDF surface and increased its hydrophilicity. Compared to the pristine PVDF membrane (-70.9 ± 3 mV), the PVDF/PDA selective layer showed a higher negatively charge (-89.1 ± 5 mV) due to the existing functional groups in the PDA. The 3D printed support has the highest roughness value (R_a = 190 ± 15 nm) which can be related to MultiJet Printing (MJP) technology used by the 3D printer which deposits the building material layer by layer on the top of each other, resulting in a rough surface [17]. The roughness of the 3D wavy composite membrane is the same as that of the PVDF/PDA selective layer, confirming the formation of a continuous, uniform coating onto the 3D printed support.

Table 1. Physical properties of the 3D support, pristine PVDF, PVDF/PDA selective layer and 3D wavy composite membrane

Membrane	Contact angle (°)	Surface Zeta Potential (mV)[(a)]	Roughness parameters (nm)	
			R_a	R_{RMS}
3D support	85 ± 2	----------	251 ± 15	----------
Pristine PVDF	93 ± 2	-70.9 ± 3	22.7 ± 0.6	29.7 ± 0.6
PVDF/PDA selective layer	51 ± 3	-89.1 ± 5	90.1 ± 8.0	121.7 ± 9.7
3D wavy composite membrane	51 ± 3	-89.1 ± 5	90.1 ± 8.0	121.7 ± 9.7

[(a)]The surface zeta potential was measured at pH = 7.0.

3.3. Filtration performance and CP characterisation

The 3D wavy composite membranes prepared using pristine PVDF had a pure water permeance (PWP) of 41 ± 1.5 LMH bar^{-1} and 67% rejection for RB5 (MW = 991 Da), showing UF performance. The PWP for wavy and flat composite membranes prepared from PVDF/PDA selective layer are 14 ± 2 LMH bar^{-1} and 10 ± 2 LMH bar^{-1}, respectively (**Figure 7a**, at time 0). The higher PWP for wavy membranes is attributed to two factors: first, a ~20% larger surface area compared to the flat one, even though they have the same footprint (50 mm). This can be considered as one additional advantage of manufacturing patterned membranes using 3D printing compared to conventional techniques, where the size and the number of pores does not reduce due to the printer's high resolution [36]. Second, a reduced thickness of the laminar sub-layer near the membrane surface due to turbulence/eddies caused by the wavy structure, as evidenced by the reduced fouling build-up (**Figure 8**). When the feed was switched to dye solution, permeance decreased due to concentration polarisation, reaching steady state after ~5 minutes of permeation, with the wavy membrane showing a lower flux decline than the flat one (**Figure 7a**). This behaviour is consistent with BSA fouling tests on flat and wavy 3D printed UF composite membranes [18]. The NF performance of the wavy composite membranes was evaluated via rejection of a series of dyes, including RB5, CR, AR1 and MO, with different molecular weights at 2 bar and feed concentration of 0.01 g L^{-1} (**Figure 7b**). RB5 and CR dyes exhibited a high rejection of > 94%, AR1 had a slightly lower rejection of 88%, and MO had a low rejection of 50%. The mass balance for all rejection tests was above 97%, signalling that the adsorption of the dyes onto the membranes was negligible. The main rejection mechanisms in NF membranes are size (steric) exclusion and Donnan (charge) exclusion [37, 38]. As both the composite membranes (**Table 1**) and the dyes tested have negative charge, it can be assumed that the dominant factor is size sieving. Since RB5, CR and AR1 have larger molecular sizes compared to MO, high resistance of the former dyes results in their high rejection in the filtration tests. The flat composite membranes prepared from PVDF/PDA selective layer showed similar dye rejection to the wavy composite membranes due to the fact that the rejection performance is attributed to the selective layer only [39]. The MWCO value of the flat and wavy composite membrane is determined to be around ~550 Da. Calibration curves for the dye rejection measurements are presented in **Figure S4**.

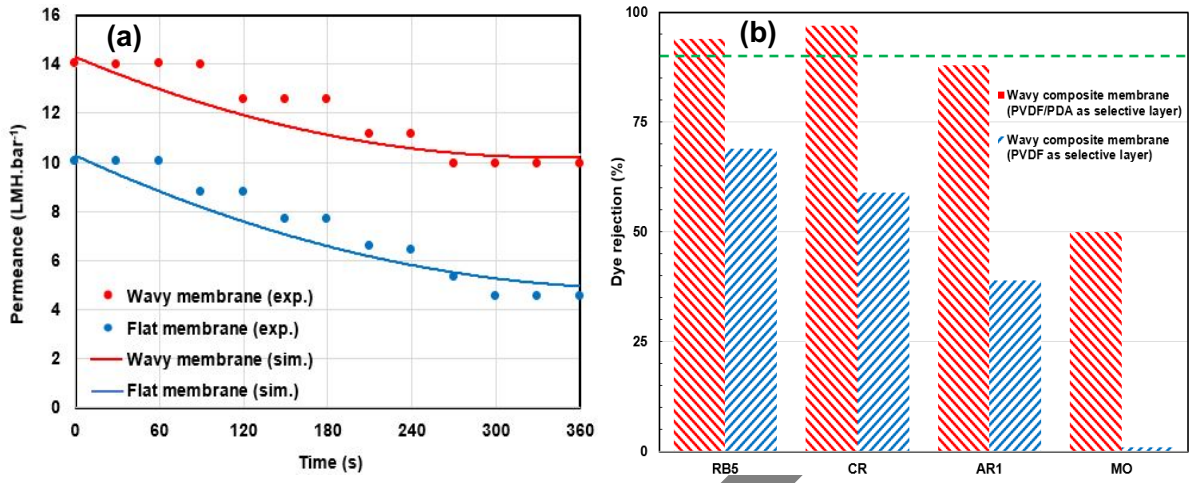

Figure 7. (a) Dye solution permeance decline for the first 5 minutes of permeation for wavy and flat membranes: dots report experimental data points, whereas the continuous line comes from CFD simulations; (b) Dye rejection performance of the wavy composite membranes prepared from pristine PVDF and PVDF/PDA as selective layers at 2 bar and inlet concentrations of 0.01 g L^{-1}. RB5: reactive black 5; CR: Congo red; AR1: acid red 1; MO: methyl orange. The mass balance for all the filtration experiments was > 97% (green dotted line refers to 90% rejection).

Concentration polarisation is governed by two simultaneous processes: (1) convective transport of particles towards the membrane along with the permeate flow and (2) back-transport of particles from the concentrated layer into the bulk phase [40]. As such, the extent of CP can be quantified by using the solute concentration at the membrane surface, the mass transfer coefficient k and the CP factor [41]. A lower solute concentration at the membrane surface means a higher k value and, therefore, lower CP. To calculate k (equation (4)), the solute concentration at the membrane surface (C_m) is needed, but this cannot be easily measured experimentally [42]. On the other hand, CFD simulations have been effectively used to calculate solute concentrations at the membrane surface, with high accuracy and reliability [43-45]. CFD simulation results can be very accurate if the conservation of mass and momentum along with mass transport equations are solved under laminar flow conditions [42, 46]. In this work, the CFD simulations were performed at TMP of 2 bar and Re = 700 to determine the maximum CR (solute) concentration at the surface of flat and wavy composite membranes. Results confirm that the CFD permeance curves accurately model experimental data (**Figure 7a**). Further details of the model development can be found in the **Supporting Information**. The steady state fluxes of CR dye solution (0.01 g L^{-1}) at 2 bar for the wavy and flat membranes

are 20 LMH and 10 LMH, respectively (**Table S1**). The maximum CR concentration (C_m), mass transfer coefficient *k* and CP factor as a function of filtration time for flat and wavy composite membranes are shown in **Figure 8 (a – c)**. C_m increases with time and reached a steady state after 300 s, with values of 0.17 g L^{-1} on the flat surface and 0.08 g L^{-1} on the wavy surface. The steady state is given by a balance between solute flow to the membrane surface, solute flux through the membrane and backflow from the surface to the bulk. A lower C_m value indicates that a higher mass transfer coefficient was achieved for the wavy membrane compared to the flat one (**Figure 8 (b)**). The CP factor for the wavy membrane is consistently lower than that of the corresponding time on the flat membrane in all instances (**Figure 8 (c)**). A quantitative comparison between wavy and flat composite membranes in terms of *k* and CP factor is reported in **Figure 8 (d)**, showing that the final (at t = 300 s) mass transfer coefficient of the wavy membrane (2.7×10^{-6} m/s) is nearly triple that of the flat membrane (1.0×10^{-6} m/s), with the CP factor being 57% lower on the wavy surface. The data and calculations for these values are reported in **Table S1**. As CP depends on various parameters such as feed solution, feed concentration, membrane type, crossflow velocity and transmembrane pressure [1], comparison with the literature is challenging. In the case of patterned membranes, this is made more complex by considerations about which area to use, i.e. the membrane's footprint (in the present case the wavy and flat membranes having the same) or the effective filtration area (in the present case the wavy membrane has ~20% larger effective filtration area than the flat one). The approaches vary in the literature, but most consider the footprint as this coincides with the membrane's module [10, 18, 41]. On this basis, the increase in mass transfer coefficient and reduction in CP factor obtained in this work are very similar to values obtained via CFD for a patterned membrane with a cambered structure, reporting a x3 increase for mass transfers and a 50% reduction in CP factor for Rhodamine 6G [41]. A higher permeance coupled with a significant reduction in CP was also observed for micropatterned membranes using NaCl [10], whereas no increase in permeance was associated with reduced colloidal fouling for a nanoimprinted UF membrane [15]. It is worth mentioning that the osmotic pressure difference ($\Delta\pi$) of the Congo red solution, due to the low CR concentration, is negligible **(Supporting Information**).

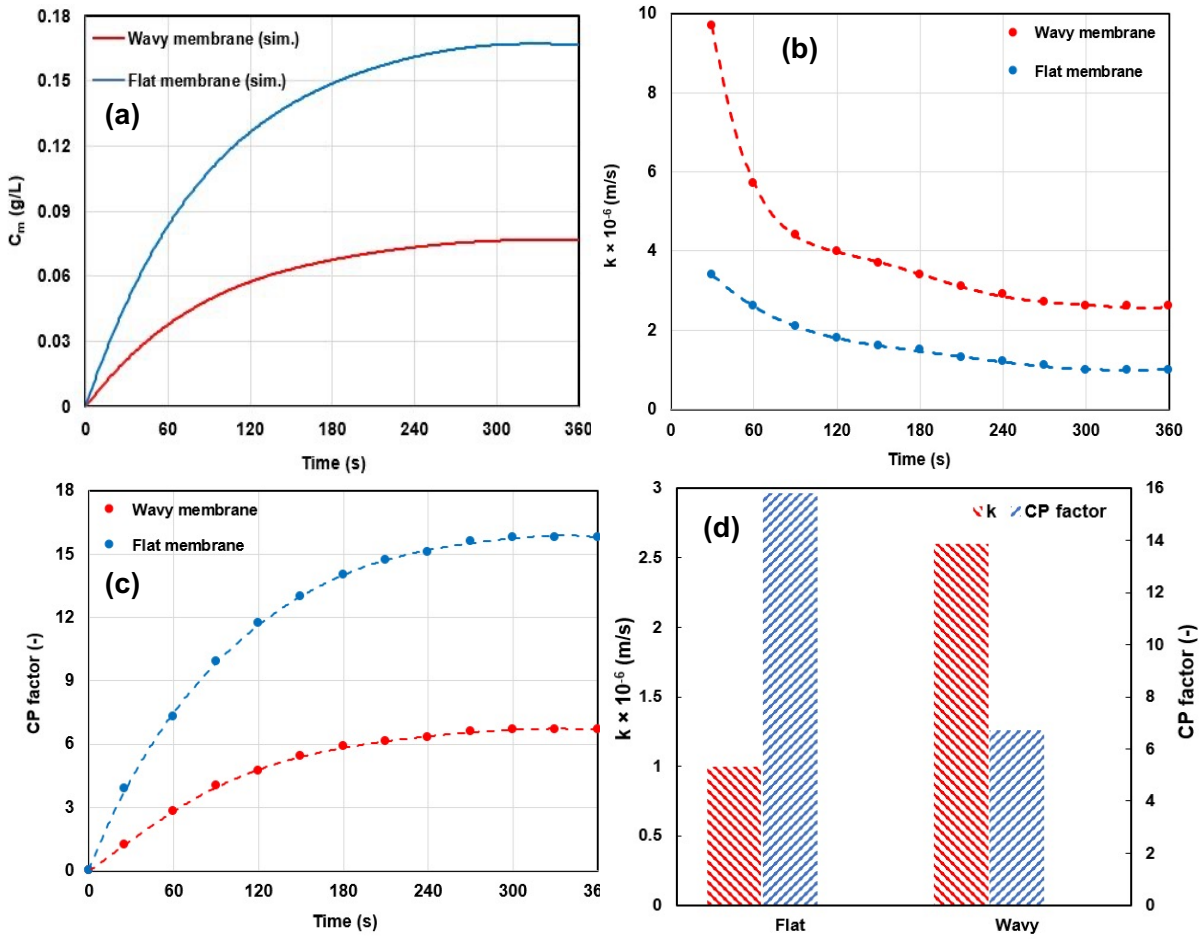

Figure 8. Time-dependent (a) maximum solute concentration at the membrane's surface; (b) mass transfer coefficient; (c) CP factor along with (d) quantitative comparison of wavy and flat composite membranes at TMP of 2 bar under *Re* = 700.

This divergent behaviour can be explained by analysing the shear stress over the wavy and flat composite membranes determined from CFD simulations (**Figure 9**), as the hydrodynamic conditions around the membrane surface can have a significant effect on CP. In fact, there is strong evidence in the literature that shear stress plays an important role in suppressing the formation of concentration polarization formation [41, 47-49]. It can be observed from **Figure 9** that the maximum shear stress increase by an order of magnitude, from 0.18 Pa on the flat surface to 1.35 Pa on the wavy surface. It is worth mentioning that *Re* = 700 was chosen so that the shear stress on the surface of the wavy membrane is within the range (0 - 1.5 Pa) used in NF membranes for industrial wastewater treatment [50]. Higher *Re* values would have further enhanced the effects of the wavy structure. The wavy structure induces a non-uniform shear stress distribution on the membrane surface where high shear stress/rate values occur at the

peaks and low shear stress/rate values occur in the valleys of the wavy structure. The average shear stress on the wavy membrane is also larger than the flat counterpart. In the presence of a higher shear stress gradient, there is a net migration of dye in the direction of a lower shear rate. The presence of flow recirculating regions in the valleys also makes the laminar sub-layer near the membrane thinner, thus reducing the overall flow resistance at the membrane surface. The shear stress values presented in **Figure 9** represent the maximum shear stress at the peaks for the wavy structures.

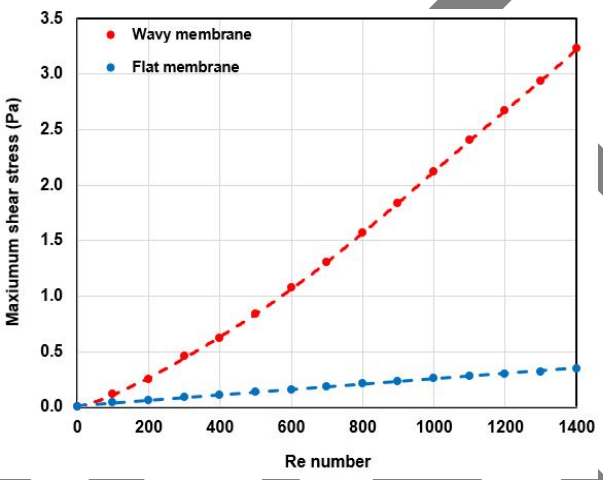

Figure 9. The maximum surface shear stress vs. Re number for wavy and flat composite membranes obtained from CVF simulations.

The energy requirement during filtration was characterised using the pressure drop incurred along the membrane. Any difference between the flat and wavy membranes was below the accuracy of the pressure gauges used experimentally (±0.01 bar). CFD simulations reported a pressure drop per unit length of ~0 and 2*10-5 $Pa*m^{-1}$, for the flat and wavy membranes, respectively. This negligible difference is to be expected given the laminar flow condition, i.e. *Re* = 700, employed in this study, and suggests that any additional energy consumption for wavy membranes is outweighed by its improved performance in permeance and concentration polarisation. It is, however, reasonable to expect the pressure drop caused by the wavy structure to be higher at turbulent flow conditions, thus diminishing somewhat its more favourable filtration properties. On the other hand, the reduction in concentration polarisation build up would increase the operating time between cleaning cycles, leading to an overall reduced downtime and resource requirement, as shown for UF membranes [14]. The authors have

shown that wavy UF membranes retain up to 87% of their initial pure water permeance after 10 complete fouling cycles.

These results show that the impact of CP in NF membranes could be effectively reduced by using 3D printed composite membranes designed to control hydrodynamics (i.e., shear stress and flow patterns) over the membrane surface.

4. Conclusion

This work reports on the successful fabrication of NF composite membranes comprising 3D printed asymmetric wavy and flat support and NF PVDF/PDA selective layers prepared by coating PDA over the UF PVDF membranes. The dye rejection results showed a high CR dye rejection (> 95%) for both membranes. The MWCO of the composite membranes was determined to be ~550 Da. The wavy structure resulted in an increase of 40% in pure water permeance due to a 20% larger surface area for the same footprint and reduced CP. The wavy structure nearly tripled the mass transfer coefficient and reduced concentration polarization by 57%. This major reduction was related to the higher shear stress on the membrane's surface, with an order of magnitude increase passing from a flat to a wavy structure. As concentration polarisation remains a major challenge in nanofiltration, these results demonstrate that 3D printing represents a viable technology route to improving the performance of nanofiltration membranes in a wide range of applications.

Authorship contributions

The manuscript was written through contributions of all authors.

Acknowledgement

The authors thank UK EPSRC for support (grant EP/M01486X/1). All data used in the manuscript is reported in the SI document.

References

1. She, Q., et al., *Membrane fouling in osmotically driven membrane processes: A review.* Journal of Membrane Science, 2016. **499**: p. 201-233.
2. Curcio, E., et al., *Membrane technologies for seawater desalination and brackish water treatment*, in *Advances in Membrane Technologies for Water Treatment*. 2015, Elsevier. p. 411-441.
3. Antony, A., et al., *Scale formation and control in high pressure membrane water treatment systems: a review.* Journal of membrane science, 2011. **383**(1-2): p. 1-16.
4. Shirazi, S., C.-J. Lin, and D. Chen, *Inorganic fouling of pressure-driven membrane processes—A critical review.* Desalination, 2010. **250**(1): p. 236-248.
5. Tang, C.Y., T. Chong, and A.G. Fane, *Colloidal interactions and fouling of NF and RO membranes: a review.* Advances in colloid and interface science, 2011. **164**(1-2): p. 126-143.
6. Rana, D. and T. Matsuura, *Surface modifications for antifouling membranes.* Chemical reviews, 2010. **110**(4): p. 2448-2471.
7. Kochkodan, V., D.J. Johnson, and N. Hilal, *Polymeric membranes: Surface modification for minimizing (bio) colloidal fouling.* Advances in colloid and interface science, 2014. **206**: p. 116-140.
8. An, Q.-F., et al., *Study on a novel nanofiltration membrane prepared by interfacial polymerization with zwitterionic amine monomers.* Journal of membrane science, 2013. **431**: p. 171-179.
9. Warsinger, D.M., et al., *A review of polymeric membranes and processes for potable water reuse.* Progress in polymer science, 2018. **81**: p. 209-237.
10. ElSherbiny, I.M., A.S. Khalil, and M. Ulbricht, *Surface micro-patterning as a promising platform towards novel polyamide thin-film composite membranes of superior performance.* Journal of Membrane Science, 2017. **529**: p. 11-22.
11. Jeffree, M.A., et al., *Gel Layer Limited Haemofiltration Rates can be Increased by Vortex Mixing.* Clinical and Experimental Dialysis and Apheresis, 1981. **5**(4): p. 373-380.
12. Heinz, O., et al., *Surface-patterning of polymeric membranes: fabrication and performance.* Current opinion in chemical engineering, 2018. **20**: p. 1-12.
13. Choi, D.-C., et al., *Effect of pattern shape on the initial deposition of particles in the aqueous phase on patterned membranes during crossflow filtration.* Environmental Science & Technology Letters, 2017. **4**(2): p. 66-70.
14. Scott, K., et al., *Intensified membrane filtration with corrugated membranes.* Journal of Membrane Science, 2000. **173**(1): p. 1-16.
15. Maruf, S.H., et al., *Use of nanoimprinted surface patterns to mitigate colloidal deposition on ultrafiltration membranes.* Journal of membrane science, 2013. **428**: p. 598-607.
16. Tijing, L.D., et al., *3D printing for membrane separation, desalination and water treatment.* Applied Materials Today, 2020. **18**: p. 100486.
17. Low, Z.-X., et al., *Perspective on 3D printing of separation membranes and comparison to related unconventional fabrication techniques.* Journal of Membrane Science, 2017. **523**: p. 596-613.
18. Mazinani, S., et al., *3D printed fouling-resistant composite membranes.* ACS applied materials & interfaces, 2019. **11**(29): p. 26373-26383.
19. Liu, F., et al., *Progress in the production and modification of PVDF membranes.* Journal of membrane science, 2011. **375**(1-2): p. 1-27.
20. Kang, G.-d. and Y.-m. Cao, *Application and modification of poly (vinylidene fluoride)(PVDF) membranes–a review.* Journal of membrane science, 2014. **463**: p. 145-165.
21. Xi, Z.-Y., et al., *A facile method of surface modification for hydrophobic polymer membranes based on the adhesive behavior of poly (DOPA) and poly (dopamine).* Journal of Membrane Science, 2009. **327**(1-2): p. 244-253.

22. Jiang, J.-H., et al., *Improved hydrodynamic permeability and antifouling properties of poly (vinylidene fluoride) membranes using polydopamine nanoparticles as additives.* Journal of membrane science, 2014. **457**: p. 73-81.
23. Xiang, Y., F. Liu, and L. Xue, *Under seawater superoleophobic PVDF membrane inspired by polydopamine for efficient oil/seawater separation.* Journal of membrane science, 2015. **476**: p. 321-329.
24. Al-Shimmery, A., et al., *3D printed composite membranes with enhanced anti-fouling behaviour.* Journal of membrane science, 2019. **574**: p. 76-85.
25. Lee, H., et al., *Mussel-inspired surface chemistry for multifunctional coatings.* science, 2007. **318**(5849): p. 426-430.
26. Yao, L., et al., *Codeposition of polydopamine and zwitterionic polymer on membrane surface with enhanced stability and antibiofouling property.* Langmuir, 2018. **35**(5): p. 1430-1439.
27. Zydney, A.L., *Stagnant film model for concentration polarization in membrane systems.* Journal of Membrane Science, 1997. **130**(1): p. 275-281.
28. Baitalow, K., et al., *A mini-module with built-in spacers for high-throughput ultrafiltration.* Journal of Membrane Science, 2021. **637**: p. 119602.
29. Lee, Y.K., et al., *Flow analysis and fouling on the patterned membrane surface.* Journal of Membrane Science, 2013. **427**: p. 320-325.
30. Kotsilkova, R., et al., *Tensile and surface mechanical properties of polyethersulphone (pes) and polyvinylidene fluoride (PVDF) membranes.* Journal of Theoretical and Applied Mechanics, 2018. **48**(3): p. 85-99.
31. Yuan, S., et al., *Super-hydrophobic 3D printed polysulfone membranes with a switchable wettability by self-assembled candle soot for efficient gravity-driven oil/water separation.* Journal of Materials Chemistry A, 2017. **5**(48): p. 25401-25409.
32. Wang, J., et al., *High flux electroneutral loose nanofiltration membranes based on rapid deposition of polydopamine/polyethyleneimine.* Journal of Materials Chemistry A, 2017. **5**(28): p. 14847-14857.
33. Liu, F., et al., *Surface immobilization of polymer brushes onto porous poly (vinylidene fluoride) membrane by electron beam to improve the hydrophilicity and fouling resistance.* Polymer, 2007. **48**(10): p. 2910-2918.
34. Ma, Z., et al., *Functional surface modification of PVDF membrane for chemical pulse cleaning.* Journal of membrane science, 2017. **524**: p. 389-399.
35. Zhao, J., et al., *Manipulating the interfacial interactions of composite membranes via a mussel-inspired approach for enhanced separation selectivity.* Journal of Materials Chemistry A, 2015. **3**(39): p. 19980-19988.
36. Maruf, S.H., et al., *Critical flux of surface-patterned ultrafiltration membranes during cross-flow filtration of colloidal particles.* Journal of membrane science, 2014. **471**: p. 65-71.
37. Nagy, E., *Basic equations of mass transport through a membrane layer*. 2018: Elsevier.
38. Koyuncu, I. and D. Topacik, *Effect of organic ion on the separation of salts by nanofiltration membranes.* Journal of Membrane Science, 2002. **195**(2): p. 247-263.
39. Baker, R.W., *Membrane technology and applications*. 2012: John Wiley & Sons.
40. Kromkamp, J., et al., *Shear-induced diffusion model for microfiltration of polydisperse suspensions.* Desalination, 2002. **146**(1): p. 63-68.
41. Shang, W., et al., *Effective suppression of concentration polarization by nanofiltration membrane surface pattern manipulation: Numerical modeling based on LIF visualization.* Journal of Membrane Science, 2021. **622**: p. 119021.
42. Santos, J., et al., *Investigation of flow patterns and mass transfer in membrane module channels filled with flow-aligned spacers using computational fluid dynamics (CFD).* Journal of Membrane Science, 2007. **305**(1-2): p. 103-117.

43. Amokrane, M., et al., *A study of flow field and concentration polarization evolution in membrane channels with two-dimensional spacers during water desalination.* Journal of membrane science, 2015. **477**: p. 139-150.
44. Ahmad, A.L., et al., *Integrated CFD simulation of concentration polarization in narrow membrane channel.* Computers & chemical engineering, 2005. **29**(10): p. 2087-2095.
45. de Pinho, M.N., V. Semião, and V.t. Geraldes, *Integrated modeling of transport processes in fluid/nanofiltration membrane systems.* Journal of Membrane Science, 2002. **206**(1-2): p. 189-200.
46. Schlichting, H. and K. Gersten, *Boundary-layer theory*. 2016: Springer.
47. Ding, A., et al., *Impact of aeration shear stress on permeate flux and fouling layer properties in a low pressure membrane bioreactor for the treatment of grey water.* Journal of Membrane Science, 2016. **510**: p. 382-390.
48. Liu, X., et al., *CFD modelling of uneven flows behaviour in flat-sheet membrane bioreactors: From bubble generation to shear stress distribution.* Journal of Membrane Science, 2019. **570-571**: p. 146-155.
49. Chan, C.C.V., P.R. Bérubé, and E.R. Hall, *Relationship between types of surface shear stress profiles and membrane fouling.* Water Research, 2011. **45**(19): p. 6403-6416.
50. Du, X., et al., *Shear stress in a pressure-driven membrane system and its impact on membrane fouling from a hydrodynamic condition perspective: a review.* Journal of Chemical Technology & Biotechnology, 2017. **92**(3): p. 463-478.